

## Article

# Hybrid Steel Fiber of Rigid Pavements: A 3D Finite Element and Parametric Analysis

Bakhtiyar Q. Khawaja Al Harki <sup>1</sup>, Mohammed S. Al Jawahery <sup>1,2,\*</sup>  and Ayman A. Abdulmawjoud <sup>3</sup> 

<sup>1</sup> Highways and Bridges Engineering Department, Technical College of Engineering, Duhok Polytechnic University, Duhok 42001, Iraq

<sup>2</sup> Department of Construction Engineering and Projects Management, Al-Noor University College, Nineveh 41012, Iraq

<sup>3</sup> Civil Engineering Department, College of Engineering, University of Mosul, Mosul 41002, Iraq

\* Correspondence: mohammed.shakib@dpu.edu.krd; Tel.: +964-75-0845-4001

**Abstract:** Rigid pavements have high compressive strength and low flexural strength due to the brittleness of concrete. This leads to the formation of cracks easily under the applied loads of vehicles; therefore, the design of concrete pavements usually leads to an increase in the high thicknesses. Hybrid steel fibers are used in concrete to increase flexural strength and minimize crack formation. Using concrete with steel fibers in pavements reduces the required concrete thickness. In recent decades, the application of the finite element method to predict the behavior of rigid pavements has increased. This study investigates the influence of hybrid steel fiber on the behavior of rigid pavements; a finite element modeling approach is used to simulate the case study. Several parameters are entered and investigated in this study, including the proportion mix of hybrid fiber concrete (HFC), which contains 0.2% macro synthetic fibers and 0.68, 0.8, and 0.96% of steel fibers, compressive strengths of 25, 35, and 45 MPa, slab thicknesses of 150, 200, and 250 mm, and the load of the tandem axle at the edge of mid slab on the Winkler foundation. The ATENA software package is used to perform a nonlinear finite element analysis. Thirty-six rigid specimen pavements with dimensions of 3600 × 3600 mm were modeled in this investigation. The results showed that the addition ratio (0.68 + 0.2)% of hybrid fibers is more effective in improving the load bearing capacity with a slab thickness of 150 mm and 25 MPa compressive strength.

**Keywords:** rigid pavement; hybrid fiber; finite element method; nonlinear analysis; parametric analysis



**Citation:** Al Harki, B.Q.K.; Al Jawahery, M.S.; Abdulmawjoud, A.A. Hybrid Steel Fiber of Rigid Pavements: A 3D Finite Element and Parametric Analysis. *Coatings* **2022**, *12*, 1478. <https://doi.org/10.3390/coatings12101478>

Academic Editor: Mingjing Fang

Received: 21 September 2022

Accepted: 4 October 2022

Published: 6 October 2022

**Publisher's Note:** MDPI stays neutral with regard to jurisdictional claims in published maps and institutional affiliations.



**Copyright:** © 2022 by the authors. Licensee MDPI, Basel, Switzerland. This article is an open access article distributed under the terms and conditions of the Creative Commons Attribution (CC BY) license (<https://creativecommons.org/licenses/by/4.0/>).

## 1. Introduction

Rigid pavements are recommended over flexible pavements due to their superior functionality and capacity to support heavy loads, but challenges such as cracks and faults caused by the environment and heavily loads decrease the functionality of concrete pavements [1–3]. Due to its tensile weakness, concrete fails under high vehicular loads, particularly on rigid pavements; the flexural strength of a rigid pavement plays an essential role in its ability to resist cracking under cyclic loads. Crack openings allow water ingress, damaging the pavement base and leading to larger concrete failures. This causes rapid pavement deterioration, higher maintenance costs, and decreased comfort and safety in vehicular traffic [4,5]. The addition of fibers can increase the tensile strength of concrete and eliminate the need for a large thickness of pavement [6]. Furthermore, the addition of fibers increases the concrete's impact, flexural, and tensile strength [7]. Many countries worldwide use rigid pavements, both with and without a base course. The different layers of the rigid pavement structure have different strengths and deformation properties, making it hard to evaluate in pavement engineering [8]. Studies have shown that adding fiber to concrete improves its toughness and crack resistance [9–13].

The use of fibers enhances concrete's durability and mechanical properties [14–16]. The bonding process between fiber-matrix and multi-directional fiber reinforcement min-

minizes volumetric changes, thus increasing durability. Additionally, fibers improve the durability of concrete by avoiding or reducing the rate of concrete deterioration [17–20]. This would open the way toward the cost-effective construction of rigid pavements, which is essential for underdeveloped nations. Therefore, adding fibers can improve the structural performance and properties of concrete. In general, fibers are added during the mixing process while the concrete is still new. Combining a variety of fibers may be a significant step toward reducing cracks and improving the performance of concrete. Two or more types of fibers can be combined to create a mixture that generates profits for each type of fiber in the composite [21].

Synthetic fibers are used in small amounts that offer the advantage of equal distribution as well as the high corrosion resistance, delaying the formation of initial cracks and improving concrete's early-age properties. Synthetic fibers can enhance the load-bearing capacity of members in the post-crack zone. Moreover, they improve fracture properties, impact resistance, ductility, and flexural toughness. Hybrid fibers contain two or more fibers, providing a matrix in which each type of fiber improves the specific performance of concrete's mechanical and physical properties. However, fibers are stiffer and stronger than other materials, such that steel fibers improve ultimate strength in addition to the first crack stress and increase concrete's ductility and toughness. The synthetic fibers with a lower modulus of elasticity are more flexible and control the cracking, as well as enhancing the early age properties of the matrix. It can be concluded from the literature that the combination of two types of fibers with different lengths and diameters bridge microcracks for the smaller fibers and the larger prevent the propagation of macro-cracks, which leads to enhancing the toughness of concrete [22–25].

In general, there are two types of previous studies on the effects of fiber on concrete: mechanical and numerical modeling of fiber-reinforced concrete (FRC). For the last decade, carbon steel fibers have been used in concrete [26]. Although not an alternative for reinforcement bars, steel fibers produce concrete with significantly improved plastic, shear, and ductile properties [27]. Therefore, steel fiber reinforcement concrete (SFRC) is frequently utilized in pavements subjected to heavy traffic loads. Apart from steel fibers, various researchers worldwide have worked on different fiber-reinforced concretes, stating that the mechanical characteristics of fiber-reinforced concrete are much superior to those of ordinary concrete [28]. Raza et al. 2020 [29] investigated that the fibers enhance the binder matrix's ability to resist cracking under tensile and bending loads due to their extremely high elastic modulus and tensile strength. In addition, Afroz et al. 2019 [30] found that adding 1% volumetric steel fiber to concrete increases its compressive and flexural strength by 10% and 80%, respectively. Lau et al. 2020 [31] demonstrated that adding steel fibers in rigid concrete pavements improved fatigue resistance and at least a 135% increase in fatigue cycles compared to the fatigue cycles of plain concrete.

According to Hussain et al., 2020 [32], adding 1% steel fiber to rigid pavement decreased the design thickness from 183 to 120 mm for normal strength concrete and 155 to 105 mm for high strength concrete. Abdulridha et al. 2021 [33] identified shrinkage cracking in the concrete pavement using different amounts of polypropylene fiber. They employed a testing program consisting of thirty combinations to analyze four parameters, namely cement content (300, 400, and 500) kg/m<sup>3</sup>, steel fiber (0, 0.075, and 0.15 vol.%), polypropylene fiber (0, 0.35, and 0.7% vol.%), and (0, 5, and 10%) silica fume by cement weight. The findings showed that the amount of cement used had a greater impact on concrete shrinkage cracking.

On the other hand, more emphasis has been placed on the numerical modeling of FRC in recent years. The finite-element (FE) method is a way to numerically solve problems with complex structures, loads, and materials. The 2D finite-element modeling had a lot of problems. Researchers couldn't model more than two layers above the subgrade, and only one layer on top of a Winkler could be used for temperature analysis. With the speed and power of computers, many researchers started using 3D modeling instead of traditional design methods. This was because 3D modeling had a lot of advantages over conventional

design methods, such as interface algorithms and thermal modules [34]. Tabatabaie and Barenberg (1980) created ILLI-SLAB, a more broad finite-element software still in use that was developed at the University of Illinois in the late 1970s for the structural analysis of jointed concrete pavements. ILLI-SLAB uses the same material as in previous models for thick plate elements. Using a second layer of plate elements beneath the slab can incorporate the impact of a bonded or unbonded base. Winkler's foundation is modeled on the subgrade. Comparing theoretical solutions for stresses and displacements was used to verify models created with ILLI-SLAB. The findings were well compared [35]. Tayabji et al. (1986) developed the JSLAB program to analyze pavements supported by a Winkler foundation. The model was similar to ILLI-SLAB because it used plate elements to model the slab and a bonded or unbonded foundation. Dowels were modeled using modified beam components that considered the influence of shear deformations and the concrete's elastic support. Like ILLI-SLAB, springs were used to model aggregate interlock and keyways [36].

Furthermore, Belletti et al., 2004 [37] provided experimental and numerical research on the behavior of slabs resting on a grade constructed of fiber-reinforced concrete for industrial pavements. This was accomplished in the lab by testing four FRC slabs with fibers of different volume fractions and aspect ratios. The slabs should be put on many steel springs to create a Winkler subgrade. The finite-element approach is used to simulate nonlinear fracture mechanics numerically. This extension focuses on using a more realistic rule for simulating the stiffness and strength of FRC after cracking the concrete matrix. As a result, the model included the stiffness matrix for FRC with primary and secondary cracks. Finally, experimental and finite element findings agreed well, providing useful information for design considerations. Khan et al. 2018 [38] used ANSYS software to model the concrete pavements. In FE, the concrete slab is represented by 45 solid brick elements, while the soil is characterized by spring elements. The analysis was conducted for a slab-soil combination and a wide range of loads. Elastic springs reflect "Winkler type" soil. The sub-grade reaction module was used to determine the soil stiffness. The important contribution of this research is to compare the model's stress results utilizing the finite-element method with the traditional approach of Westergaard's method and Indian Road Congress (IRC 58-200).

Under approximate edge wheel load stresses, Westergaard's equation is validated compared to those obtained using ANSYS. Zimmer et al. 2015 [39] used the software program 'ABAQUS' to simulate the bending laboratory test of steel fiber-reinforced concrete specimens. The testing machine was used to run a three-dimensional numerical model of a three-point bending test under static loads up to its maximum value. The loading frequencies were (0.5 and 1) kN/sec. Steel fibers comprise (0.0, 0.4, and 0.8%) of the (SFRC) flexural members or beam specimens. Stress, strain, and deformation were recorded, and the test was simulated using "ABAQUS." The experimental results and analytical approaches show that deflection, stress, and strain magnitudes are directly proportional to the increase in steel fiber.

In some countries, reinforcing mesh is used in the reinforcement of pavement. There are no specific parameters or specifications for determining the optimum quantity value per cubic meter. However, replacing the steel reinforcement with steel fibers or a mixture between them is proposed. Concrete pavements of different shapes and sizes can be analyzed under simple and multiple loading conditions using the finite element method (FEM) [40].

This research aims to examine the behavior of hybrid fibers in rigid concrete pavement by exposing the ideal mix ratio of hybrid fibers as well as the adequate thickness and compressive strength of concrete that gives effective performance carrying loads of vehicles.

## 2. Materials and Methods

### 2.1. Case Study Characterization

The case study was simulated using a finite element modeling method. Several parameters were entered and analyzed, including the proportion mix of hybrid fiber concrete (HFC), which contains 0.2% macro synthetic fibers and 0.68%, 0.8%, and 0.96% steel fibers, compressive strengths of 25, 35, and 45 MPa, slab thicknesses of 150, 200, and 250 mm, and the load of the tandem axle at the edge of mid slab on the Winkler foundation.

The rigid concrete pavement was tested by using nonlinear finite element analysis. Thirty-six hybrid fiber rigid pavement samples were created and designed to fail in load-carrying capacity. All rigid pavements had the same dimension in length and width, 3600 mm and 3600 mm, respectively, while the thickness was the variable. Figure 1 shows the specification and dimensions of all samples used in this study.

The edge of the mid slab is one of the most critical vehicle loading positions, as revealed by past research [41,42]. The load was supposed to be static, which is a common method to represent pavement loads. It was calculated using the equivalent contact area in the load configuration [43,44]. The distance between the front and rear tandem axles is large, and the critical pavement responses from a single tandem axle will not be affected by the other axle. Therefore, for the analysis in this study, a single tandem axle (a set of two axles) at the edge of the mid slab was selected. A square footprint was adopted, which resulted in greater agreement with finite element meshing [45], such as in Figure 1. If the vertical movement was unrestricted, the joint functioned as a free edge with a load-bearing capacity that was less than 50% of the internal regions [46,47]. The dimension of the contact area between the wheel and the slab was 23 mm  $\times$  23 mm, the distance between two axles was 1370 mm, and the distance between the center of a dualtyre was 1815 mm [41,44].

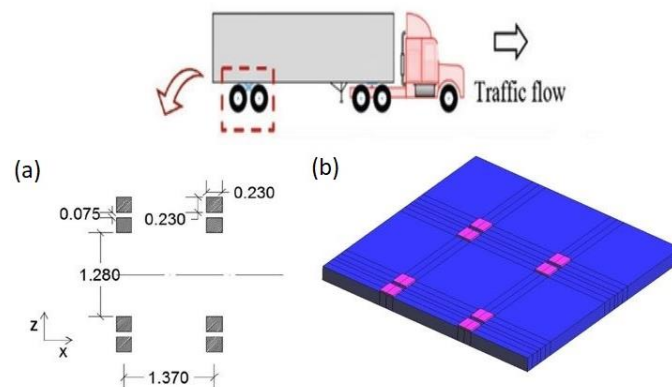


**Figure 1.** (a) Dual tyre tandem axle (b) critical load axle location [41,48].

Concrete pavements are commonly proposed as beams or plates resting on an elastic foundation. The elastic foundation for such models is represented by several hypothetical springs positioned at the bottom of the beam/plate. This study analyzes a pavement supported by a Winkler spring foundation [49–52]. According to the Winkler foundation model, the foundation is represented as a bed of linear springs that are uniformly spaced apart and independent. The model assumes that no load is transmitted to the nearby springs and that each spring deforms in response to the vertical tension applied directly to the spring. Westergaard (1926) used these pavement support systems in his study [53]. The modulus of the subgrade reaction is calculated in the field using data obtained from a plate-loading test. The modulus of the subgrade reaction of the supporting layer is theoretically equal to the spring constant utilized in the current formulation such as Figure 2. In this study, the modulus of the subgrade was 54,000 kN/m<sup>2</sup>/m for good soil to obtain the failure in the rigid slab models.

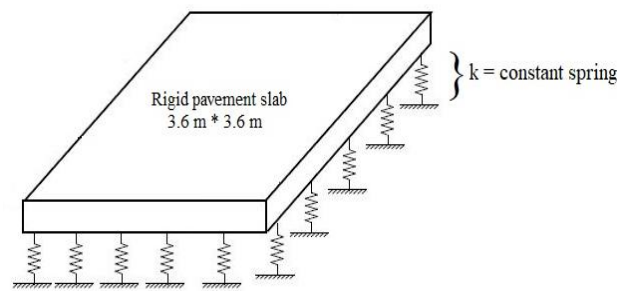


**Figure 2.** The schematization of a concrete slab on Winkler spring foundation [49].

The designation of rigid hybrid fiber concrete (RHFC) contains three terms. The first term represents the sample number (R No.), the second term represents the type of pavement: pavement control (P) or hybrid fiber (H) with a slab thickness of (150, 200, and 250), the third term represents the steel fiber ratio which is used in the mix of the sample. Table 1 shows the framework of this study with all specimens properties of FE analysis.

**Table 1.** Properties of finite element of rigid hybrid fiber concrete RHFC.

$f_c'$ (MPa)	Thickness $t$ (mm)	Hybrid Fibers (Steel Fiber + Macro-Synthetic Fiber) %			
		0	(0.68 + 0.2)%	(0.8 + 0.2)%	(0.96 + 0.2)%
25	150	R1-P150-0-25	R4-H150-0.68-25	R7-H150-0.8-25	R10-H150-0.96-25
	200	R2-P200-0-25	R5-H200-0.68-25	R8-H200-0.8-25	R11-H200-0.96-25
	250	R3-P250-0-25	R6-H250-0.68-25	R9-H250-0.8-25	R12-H250-0.96-25
35	150	R13-P150-0-35	R16-H150-0.68-35	R19-H150-0.8-35	R22-H150-0.96-35
	200	R14-P200-0-35	R17-H200-0.68-35	R20-H200-0.8-35	R23-H200-0.96-35
	250	R15-P250-0-35	R18-H250-0.68-35	R21-H250-0.8-35	R24-H250-0.96-35
45	150	R25-P150-0-45	R28-H150-0.68-45	R31-H150-0.8-45	R34-H150-0.96-45
	200	R26-P200-0-45	R29-H200-0.68-45	R32-H200-0.8-45	R35-H200-0.96-45
	250	R27-P250-0-45	R30-H250-0.68-45	R33-H250-0.8-45	R36-H250-0.96-45

## 2.2. Validation Materials

The specimens were made with hooked-type steel fibers, and the synthetic fibers used in this study had a 90-aspect ratio. The manufacturer's specifications for the fibers used are presented in Table 2.

**Table 2.** Properties of fibers as supplied by the manufacturer [22].

Steel fibers	Fiber type	-	Hooked
	Fiber length	$L_f$ (mm)	50
	Fiber diameter	$D_f$ (mm)	1.1
	Ultimate tensile strength	MPa	1100
Macro synthetic fibers	Fiber length	$L_f$ (mm)	40
	Fiber diameter	$D_f$ (mm)	0.45
	Ultimate tensile strength	MPa	620

## 2.3. Constitutive Models for Nonlinear Finite Element Analysis

The fracture-plastic model was used in this study to combine constitutive models for tensile (fracturing) and compressive (plastic) behavior. The fracture model depends on the crack band model and the orthotropic smeared-crack formulation. It uses the Rankine failure criterion and exponential softening, which may be rotated or fixed. The hardening/softening plasticity model is based on the Menétrey-Willam failure surface. The model uses the return mapping algorithm to integrate constitutive equations. The

development of an algorithm for combining the two models receives special attention. The combined algorithm is based on recursive substitution and allows the development and formulation of the two models separately. Concrete cracking, crushing under high confinement, and fracture closure lead to crushing in other material directions, which may be simulated using this mode [54].

The concrete was modeled using 3D solid hexahedron (brick) components with eight nodes (CCIsoBrick<xxxxxxx>) (code name of the brick elements in ATENA software) with (CC3DNonLinCementitious2) material that is suitable for rock or concrete-like materials. The loading plate using tandem axles dual tires at the edge of the mid slab was modeled using 3D solid hexahedron components with eight nodes (CCIsoBrick<xxxxxxx>) (code name of the brick elements in ATENA software) with CC3DElastIsotropic material, which is a linear elastic isotropic material for 3D. Spring support is a particular layer of surface elements at the boundary of the analyzed structure. Finally, contact between two surfaces was modeled using pentahedron interface components with 12 nodes. Detailed information related to the elements mentioned above can be found in the Atena manuals [54,55].

By piecewise linear relationships presented in Figure 3, the crack-normal stress components are connected to cracking strains corresponding to multiple and localized cracks opening. Multiple cracks are considered to close only when exposed to crack-normal compression (plasticity-like unloading). In contrast, a localized crack is supposed to close when normal stress reduces linearly to zero at zero [54].

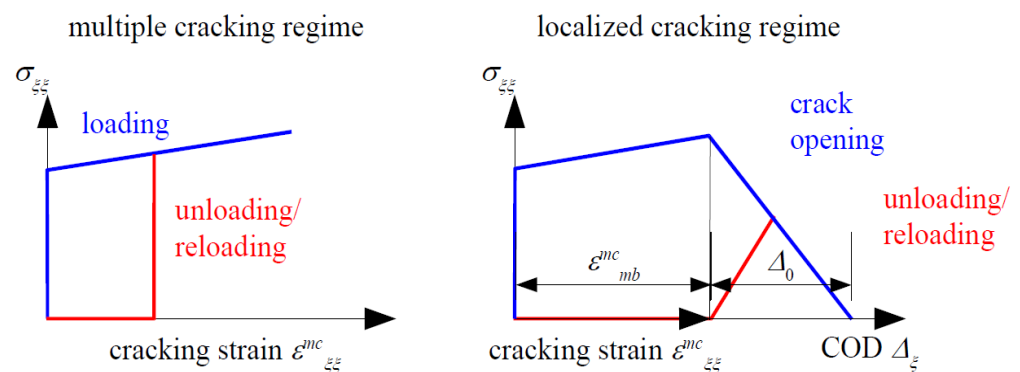


**Figure 3.** Stress vs. cracking strain relations in crack-normal direction [54].

To simulate the impact of steel fibers on the mechanical characteristics of concrete, a material model named “Cementitious2 User (FRC)” incorporated in Atena-GiD was employed. Cementitious2 User (FRC) is a useful material model for strain-hardening cementitious composites coupled with randomly oriented fibers made from diverse materials (steel, polymers, etc.) and applied in various fractions. This model employs specialized numerical models to account for FRC-specific characteristics, such as the geometry of a tensile softening branch, high toughness, and ductility. Consequently, the effect of steel fibers can be incorporated into the constitutive model of steel fiber reinforced concrete. See the ATENA Manuals for information on defining the user material response functions.

#### 2.4. Rigid Hybrid Fiber Concrete RHFC Finite Element Model

The nonlinear finite element models consist of 36 rigid pavement models with three groups in the same shape and dimension. Analysis of them was carried out via ATENA-GiD software. The GiD program was utilized for organizing data entrance of dimensions, materials, and all relevant generations, such as a meshing of models and then sending to ATENA program for the analysis. ATENA is specialized software for nonlinear finite element analysis of all types of structures created by Cervenka et al. (2017) [55]. All boundary conditions surrounding the test were assumed to simulate the reality of the test, as shown in Figure 4.

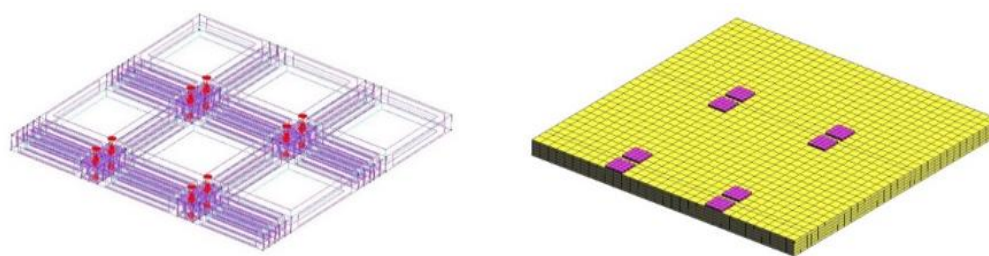


**Figure 4.** Rigid pavement boundary condition and meshing.

### 3. Results Characterization and Discussion

#### 3.1. Verification Results of Materials with the Finite Element Models

The most important crucial point is the validation of materials, which gives accuracy to the research study. The validation behavior of hybrid fiber with previous experimental results is the most fundamental part of FE modeling analysis. In this section, eight test specimens were selected from the literature to validate the behavior of hybrid fibers [22]. Four specimens of 200 mm thickness and four specimens of 250 mm thickness contained varied ratios of hybrid fiber, which contains 0.2% macro synthetic fibers and 0.68, 0.8, and 0.96% steel fibers; experimental findings were compared with data models of FE analysis. For both thicknesses, two specimens were used as a reference slab.

Table 3 displays the ultimate load capacities of experimental and FE modeling HFC slabs for 200 mm and 250 mm thickness. The correlation coefficients, standard deviation, and coefficient of variation of load capacities obtained from Figure 5 of experimental results versus the FE analysis of load for slab models were 0.957, 205.89, and 17.71, respectively; these results indicate good compatibility between the FE modeling analysis and test specimens; moreover, for further case studies, the FE modelling analysis can be predicted precisely with acceptable error.

**Table 3.** Displays the specimen results of ultimate load for experimental and FE models for HFC slabs 200 mm and 250 mm [22].

No.	Specimens Name	Experimental $P_{exp.}$ (kN)	Finite Element $P_{ATENA}$ (kN)
1	Reference 200	847.9	863.15
2	HFR200-0.68/0.2	978.1	1008.69
3	HFR200-0.80/0.2	1029.9	1014.63
4	HFR200-0.96/0.2	1117.6	1100.32
5	Reference 250	1147.6	1143.01
6	HFR250-0.68/0.2	1375.5	1336.8
7	HFR250-0.80/0.2	1300.2	1350.38
8	HFR250-0.96/0.2	1386.5	1486.68

#### 3.2. FE Modeling Results

The maximum load capacities under the wheel axle at the edge of the mid slab with and without hybrid fiber resulting from the finite element analyses are given in Table 4. According to Table 4, it can be concluded that there was good improvement in all parameters concerning the load capacity and mode of failure for all samples.

To interpret the effective role of each parameter thickness of the rigid slab, compressive strength ( $f_c'$ ), and hybrid fiber ratio ( $V_f\%$ ) on the mechanical behavior of rigid concrete pavement, the parametric study was carried out to verify the generalization of the proposed models and to study the influence of each parameter on the predicted value of load capacity.

The main effect plots extracted as a result of the parametric study are shown in Figure 6. These plots give further insight to researchers regarding the effect of considered parameters on the ultimate load capacity of rigid concrete pavement. The parametric analysis examines each value of  $t$ ,  $f_c'$ , and  $V_f\%$ . The minimum and maximum values of each parameter

are utilized as identified by the FE database. It can be determined from Figure 6 that all considered parameters significantly influence the load capacity of the rigid pavement. However, the impact of hybrid fiber ratio on the load capacity is the highest among all considered, especially at (0.68 + 0.02)% of hybrid fiber content, and this impact decreases gradually as the hybrid fiber content increases.

**Table 4.** Ultimate axle load capacity at the edge of mid slab Pu (kN) and improvement rate.

$f_c'$ (MPa)	Thickness t (mm)	Hybrid Fibers (Steel Fiber + Macro-Synthetic Fiber) %						
		0%	(0.68 + 0.02)%	Improvement Rate %	(0.8 + 0.2)%	Improvement Rate %	(0.96 + 0.2)%	Improvement Rate %
25	150	140.17	241.79	72.50%	233.12	66.3%	221.04	57.7%
	200	228.28	356.01	55.90%	300.91	31.8%	296.76	30.0%
	250	282.73	437.6	54.80%	425.71	50.6%	418.53	48.0%
35	150	178.38	284.35	59.40%	273.1	53.1%	271.19	52.0%
	200	278.41	416.08	49.40%	378.12	35.8%	366.22	31.5%
	250	365.26	543.56	48.80%	514.45	40.8%	500.84	37.1%
45	150	235.06	337.74	43.70%	330.3	28.6%	300.98	30.0%
	200	330.61	457.43	38.40%	437.6	32.4%	434.38	31.4%
	250	433.51	618.73	42.70%	590.67	36.2%	578.19	33.4%

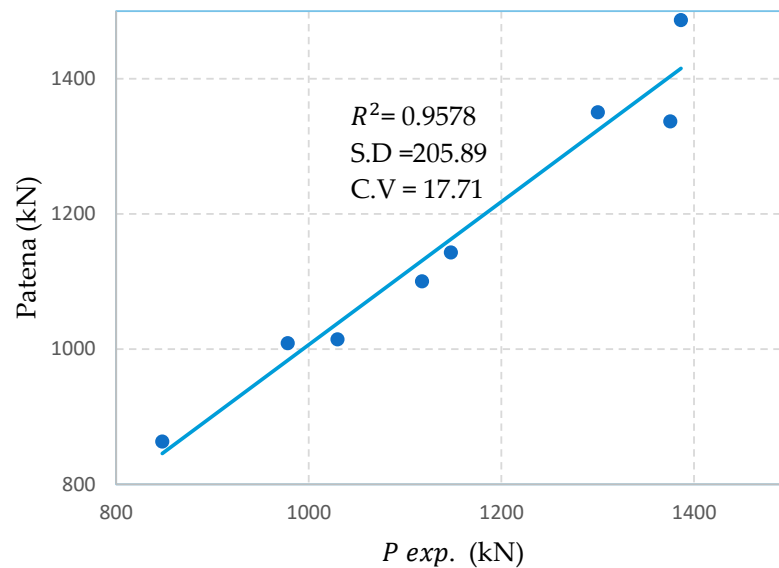


**Figure 5.** Experimental results versus the FE analysis of load for slab models [22].

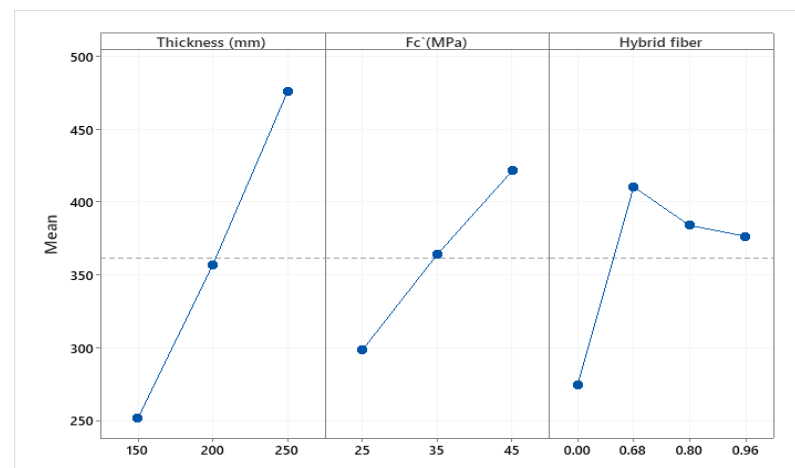


**Figure 6.** Main effects plot for ultimate load capacity Pu (kN).



Moreover, a remarkable effect is observed on the load capacity when compressive strength values are between (25 MPa to 35 MPa). However, less influence is observed when the range of  $f_c'$  is between (35 MPa to 45 MPa).

Interaction diagrams extracted as a result of the parametric study shown in Figure 7 compare the proportional effect of each parameter on the load capacity of RHFC pavement comprehensively. According to Figure 7, it can be concluded that the interaction graphs are compatible with the outcomes of the main effect plots. As shown in Figure 7, all combinations of the parameters ( $V_f$ ,  $f_c'$ , and  $t$ ) are sketched in two-dimensional spaces concerning the essential parameter of ultimate load capacity ( $P_u$ ). It is easy to see the roles of each parameter on the main parameter ( $P_u$ ) with a significant increase in the value of ( $P_u$ ) when the other values of parameters increased in all cases of the 2D parametric analysis. When all the graphs are analyzed, it can be seen that there are no extraordinary values that disarrange the trend of changes between parameters. This condition also proves the reliability and accuracy of the parametric analysis.

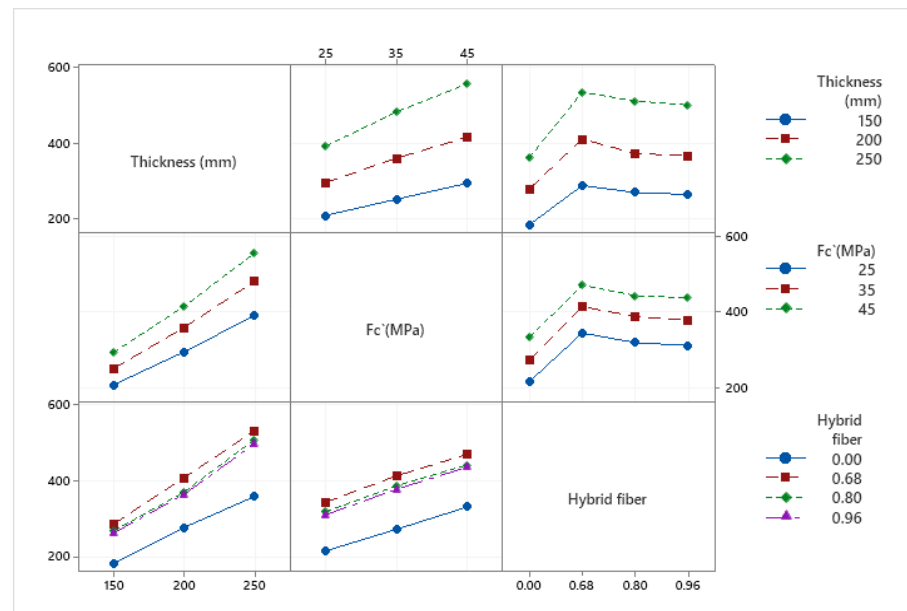


**Figure 7.** Interaction plot for ultimate load capacity  $P_u$  (kN).

### 3.3. Parametric Study on the RHFC Pavement

The effective role of the hybrid fiber ratio on the load-deflection relationship of all proposed hybrid fiber rigid pavement groups can be observed in Table A1 in the Appendix A, comparing the curves concerning the hybrid fiber ratios when keeping other parameters constant. It can be concluded from the curves that the effective ratio of hybrid fiber is 0.2% macro synthetic fibers and 0.68% steel fibers, which increases the load capacity and ductility more than other ratios. It can also be concluded that the existence of hybrid fiber increases the ductility of a rigid pavement. Moreover, an increase in the hybrid fiber ratio decreases the deformation capability. This result can be attributed to the bridging effect of hybrid fiber, which tries to prevent crack propagation. As expected, as the hybrid fiber ratio increases, the load capacities of all rigid slabs increase. However, it can be noted that hybrid fiber positively affects the load capacity.

As mentioned above, adding (0.68 + 0.2)% of the hybrid steel fiber ratio is more effective in improving load-bearing capacity with a slab thickness of 150 mm at 25 MPa compressive strength, which is about 72.5 from Table 4.

According to Sorelli et al. [56], the low content of steel fibers effectively increases the load-carrying capacity of slabs on the ground. It makes the structural response more ductile; therefore, a volume fraction of steel fibers greater than 0.68% slightly increases the ultimate load but significantly increases the slab ductility. Using more than 0.68% regularly

is not economical, and the decrease in load bearing capacity is that the fibers spreading, with a high fiber percentage in the concrete, are very difficult and thus contribute to a reduction in workability and incomplete consolidation, according to Shakir et al. [57].

As well as Table 4, Figures 6 and 7 show the ultimate interaction and main effect plot for the ultimate load-deflection relationship exhibiting the effective role of compressive strength at the load capacity when it increases from 25, 35, and 45 MPa, as well as keeping other parameters constant. The main effect for ultimate load capacity shows that the load capacity increases about 22% when the compressive strength increases from 25 to 35 MPa and increases approximately 15.72% when the compressive strength increases from 35 to 45 MPa with less slight effect.

The load-carrying capacity of RHFC slabs was also increased by increasing the thickness of the slab. The influence of hybrid steel fiber content is based not only on hybrid fiber content and compressive strength but also on the thickness of the slab. The main effect for ultimate load capacity shows that the load capacity increases about 44% when the thickness of the slab increases from 150 mm to 200 mm and increases approximately 31.5% when the thickness of the slab increases from 200 mm to 250 mm.

The cracks pattern can also be observed from graphs showing a good fit in FE analysis results regarding load-deflection relationships, as shown in Table A2 in Appendix A. However, some differences may exist between these curves. This variation may be due to the hypothesis of FE modeling, which is a perfect connection between hybrid fiber and concrete while in reality, slipping may occur between them. Moreover, it can be seen from the figures of these samples that a huge debonding crack has appeared under the wheel axle of the model.

#### 4. Conclusions

The current study explores the behavior of RHFC pavement with different ratios of hybrid fiber contents of steel and macro-synthetic fiber. These variations in hybrid fiber content are taken as a scale to measure their appropriate hybrid fiber ratio in concrete to decrease the cracking rate in rigid pavements. The work focuses on examining the effects of hybrid steel fiber volume fraction on the behavior of rigid pavements, in addition to other variables, which are the thickness of the rigid pavement and the compressive strength of concrete. The nonlinear finite element models were employed to perform this study. The programs of this study consisted of 36 models of (3600 × 3600) mm rigid concrete pavement, these models used three main variables of hybrid steel fiber ( $V_f$ ) (0.2 of macro synthetic fibers plus (0.68, 0.8, and 0.96)% of steel fiber), as well as three values of compressive strength ( $f_c'$ ) (25, 30, 35) MPa, as well as three values of thicknesses (150, 200, 250) mm. The results of the analysis were pointed out as follows:

1. Experiments have demonstrated that hybrid fiber reinforcement greatly enhances the strength and flexibility of pavements by minimizing cracking phenomena caused by loads or shrinkage effects.
2. A relatively low amount of hybrid steel fibers efficiently improves the load-carrying capacity of pavements on the ground and makes the structural behavior more ductile; volume ratios of hybrid fibers greater than (0.68 + 0.2) percent hardly improve the ultimate load but significantly improve the pavement ductility.
3. The finite element method applied in this study perfectly describes the behavior of RHFC pavement with soil under static loading.
4. The load-deflection curves of RHFC pavements containing (0.8 + 0.2)% and (0.96 + 0.2)% hybrid (steel + macro-synthetic) fiber demonstrates a slight difference in behavior. This might be retained to increase the air voids and air content of the trapped air, resulting in a loss in compressive strength.
5. The load-deflection curves of hybrid fiber-reinforced concrete pavements, which contained (0.68 and 0.2)% of hybrid (steel + macro-synthetic) fibers demonstrate a high difference in behavior, which has a significant impact on improving the characteristics of concrete.

- The most important outcome of this study is to find the ideal volumetric percentage of hybrid steel fibers with effective compressive strength and thickness values, which give a significant performance of rigid pavement, as well as the critical information that can use in the design of rigid pavement.

**Author Contributions:** Conceptualization, M.S.A.J. and A.A.A.; methodology, M.S.A.J.; software, B.Q.K.A.H. and M.S.A.J.; validation, B.Q.K.A.H., M.S.A.J. and A.A.A.; formal analysis, M.S.A.J.; investigation, B.Q.K.A.H., M.S.A.J. and A.A.A.; resources, B.Q.K.A.H.; data curation, B.Q.K.A.H.; writing—original draft preparation, B.Q.K.A.H.; writing—review and editing B.Q.K.A.H., M.S.A.J. and A.A.A.; visualization, B.Q.K.A.H.; supervision, M.S.A.J. and A.A.A.; All authors have read and agreed to the published version of the manuscript.

**Funding:** This research received no external funding.

**Institutional Review Board Statement:** Not applicable.

**Informed Consent Statement:** Not applicable.

**Data Availability Statement:** Not applicable.

**Conflicts of Interest:** The authors declare no conflict of interest.

### Appendix A

**Table A1.** Displays the load-deflection curves of rigid pavement specimens.

No.	Specimens Name	Load-Deflection Curves
1	R1-P150-0-25 R4-H150-0.68-25 R7-H150-0.8-25 R10-H150-0.96-25 $f_c$ : 25 MPa t: 150 mm	
2	R2-P200-0-25 R5-H200-0.68-25 R8-H200-0.8-25 R11-H200-0.96-25 $f_c$ : 25 MPa t: 200 mm	

Table A1. Cont.

No.	Specimens Name	Load-Deflection Curves
3	R3-P250-0-25 R6-H250-0.68-25 R9-H250-0.8-25 R12-H250-0.96-25 $f_c$ : 25 MPa $t$ : 250 mm	
4	R13-P150-0-35 R16-H150-0.68-35 R19-H150-0.8-35 R22-H150-0.96-35 $f_c$ : 35 MPa $t$ : 150 mm	
5	R14-P200-0-35 R17-H200-0.68-35 R20-H200-0.8-35 R23-H200-0.96-35 $f_c$ : 35 MPa $t$ : 200 mm	
6	R15-P250-0-35 R18-H250-0.68-35 R21-H250-0.8-35 R24-H250-0.96-35 $f_c$ : 35 MPa $t$ : 250 mm	

Table A1. Cont.

No.	Specimens Name	Load-Deflection Curves
7	R25-P150-0-45 R28-H150-0.68-45 R31-H150-0.8-45 R34-H150-0.96-45 $f_c$ : 45 MPa t: 150 mm	
8	R26-P200-0-45 R29-H200-0.68-45 R32-H200-0.8-45 R35-H200-0.96-45 $f_c$ : 45 MPa t: 200 mm	
9	R27-P250-0-45 R30-H250-0.68-45 R33-H250-0.8-45 R36-H250-0.96-45 $f_c$ : 45 MPa t: 250 mm	

Table A2. Displays the finite element cracks pattern of the rigid pavement specimens.

No.	Specimens Name	Finite Element Cracks Pattern
1	R1-P150-0-25 $f_c$ : 25 MPa t: 150 mm $V_f$ : 0%	

Table A2. Cont.

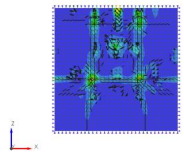
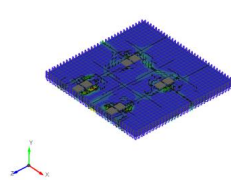
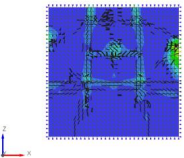
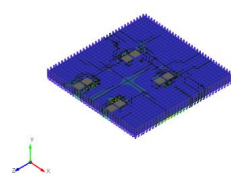
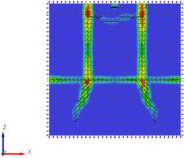
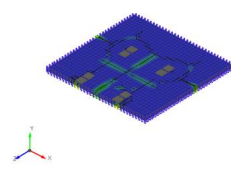
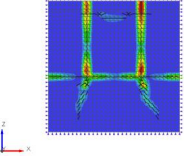
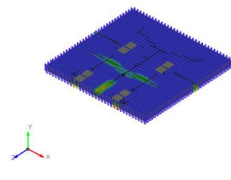
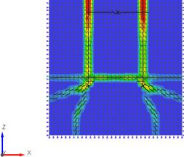
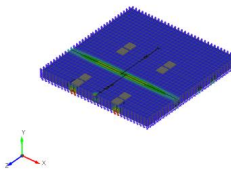
No.	Specimens Name	Finite Element Cracks Pattern	
2	R2-P200-0-25 $f_c$ : 25 MPa $t$ : 200 mm $V_f$ : 0%		
3	R3-P250-0-25 $f_c$ : 25 MPa $t$ : 250 mm $V_f$ : 0%		
4	R4-H150-0.68-25 $f_c$ : 25 MPa $t$ : 150 mm $V_f$ : 0.68 + 0.2%		
5	R5-H200-0.68-25 $f_c$ : 25 MPa $t$ : 200 mm $V_f$ : 0.68 + 0.2%		
6	R6-H250-0.68-25 $f_c$ : 25 MPa $t$ : 250 mm $V_f$ : 0.68 + 0.2%		

Table A2. Cont.

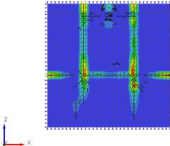
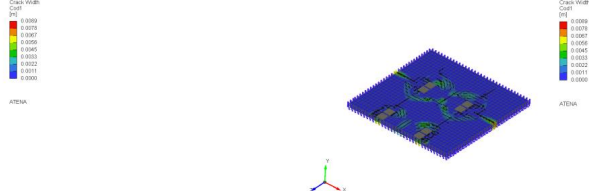
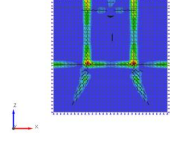
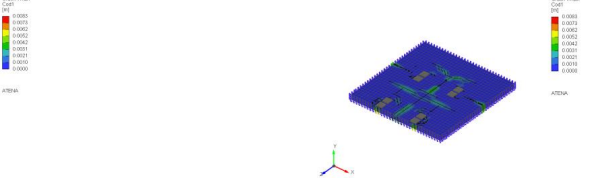
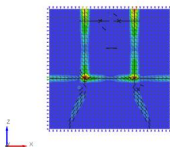
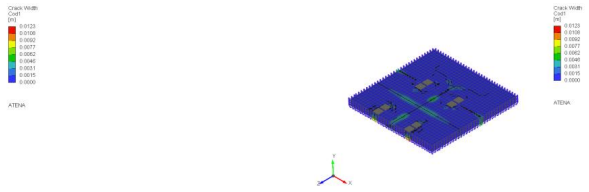
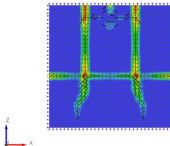
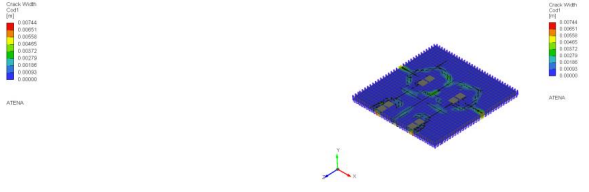
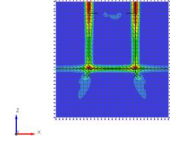
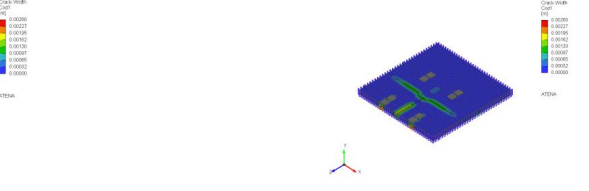
No.	Specimens Name	Finite Element Cracks Pattern	
7	R7-H150-0.8-25 $f_c$ : 25 MPa $t$ : 150 mm $V_f$ : 0.8 + 0.2%		
8	R8-H200-0.8-25 $f_c$ : 25 MPa $t$ : 200 mm $V_f$ : 0.8 + 0.2%		
9	R9-H250-0.8-25 $f_c$ : 25 MPa $t$ : 250 mm $V_f$ : 0.8 + 0.2%		
10	R10-H150-0.96-25 $f_c$ : 25 MPa $t$ : 150 mm $V_f$ : 0.96 + 0.2%		
11	R11-H200-0.96-25 $f_c$ : 25 MPa $t$ : 200 mm $V_f$ : 0.96 + 0.2%		

Table A2. Cont.

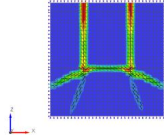
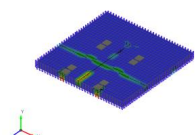
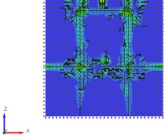
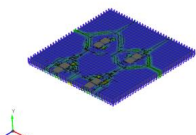
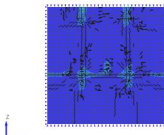
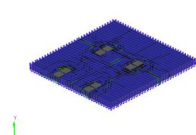
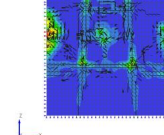
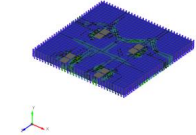
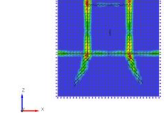
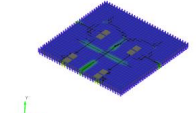
No.	Specimens Name	Finite Element Cracks Pattern	
12	R12-H250-0.96-25 $f_c$ : 25 MPa t: 250 mm $V_f$ : 0.96 + 0.2%		
13	R13-P150-0-35 $f_c$ : 35 MPa t: 150 mm $V_f$ : 0%		
14	R14-P200-0-35 $f_c$ : 35 MPa t: 200 mm $V_f$ : 0%		
15	R15-P250-0-35 $f_c$ : 35 MPa t: 250 mm $V_f$ : 0%		
16	R16-H150-0.68-35 $f_c$ : 35 MPa t: 150 mm $V_f$ : 0.68 + 0.2%		



Table A2. Cont.

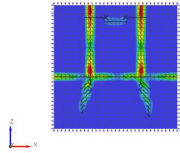
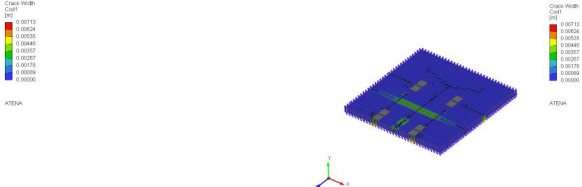
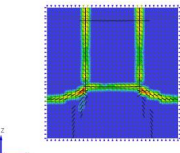
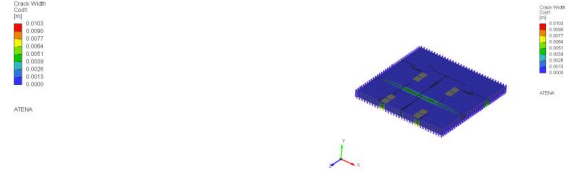
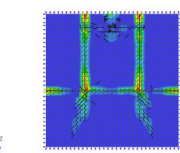
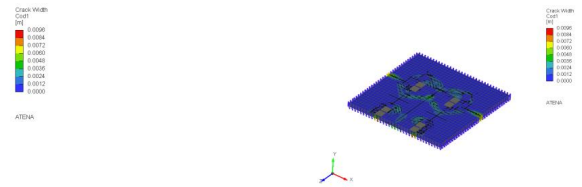
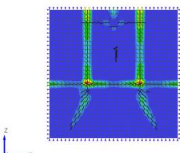
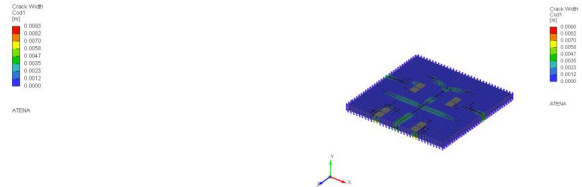
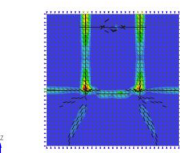
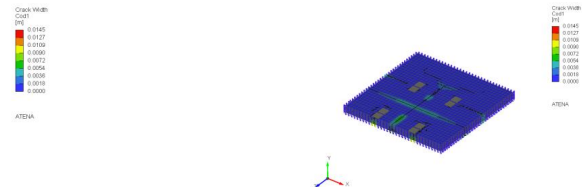
No.	Specimens Name	Finite Element Cracks Pattern	
17	R17-H200-0.68-35 $f_c$ : 35 MPa t: 200 mm $V_f$ : 0.68 + 0.2%		
18	R18-H250-0.68-35 $f_c$ : 35 MPa t: 250 mm $V_f$ : 0.68 + 0.2%		
19	R19-H150-0.8-35 $f_c$ : 35 MPa t: 150 mm $V_f$ : 0.8 + 0.2%		
20	R20-H200-0.8-35 $f_c$ : 35 MPa t: 200 mm $V_f$ : 0.8 + 0.2%		
21	R21-H250-0.8-35 $f_c$ : 35 MPa t: 250 mm $V_f$ : 0.8 + 0.2%		

Table A2. Cont.

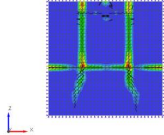
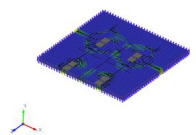
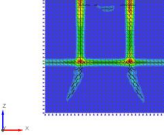
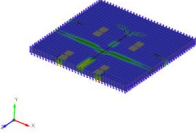
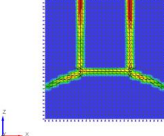
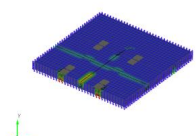
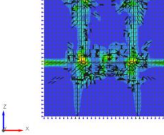
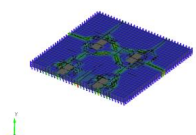
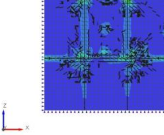
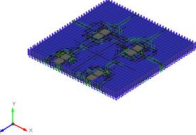
No.	Specimens Name	Finite Element Cracks Pattern	
22	R22-H150-0.96-35 $f_c$ : 35 MPa t: 150 mm $V_f$ : 0.96 + 0.2%		
23	R23-H200-0.96-35 $f_c$ : 35 MPa t: 200 mm $V_f$ : 0.96 + 0.2%		
24	R24-H250-0.96-35 $f_c$ : 35 MPa t: 250 mm $V_f$ : 0.96 + 0.2%		
25	R25-P150-0-45 $f_c$ : 45 MPa t: 150 mm $V_f$ : 0%		
26	R26-P200-0-45 $f_c$ : 45 MPa t: 200 mm $V_f$ : 0%		

Table A2. Cont.

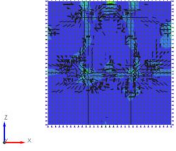
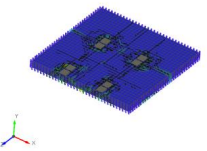
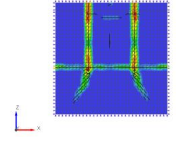
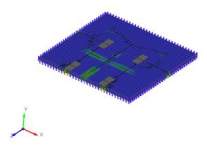
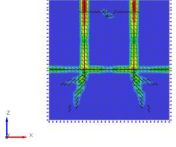
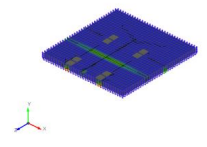
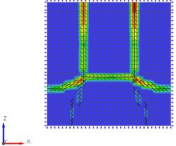
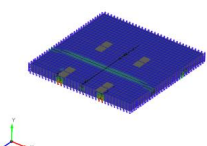
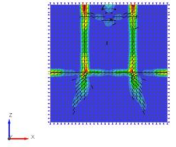
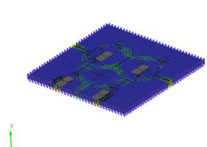
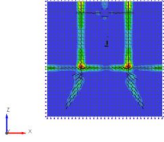
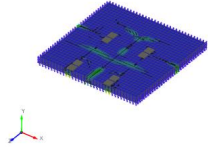
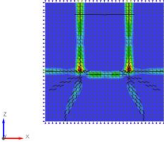
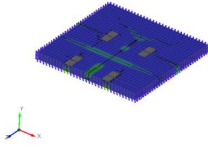
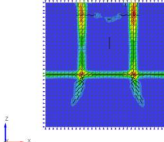
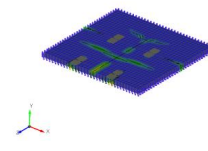
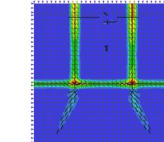
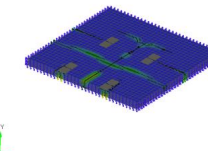
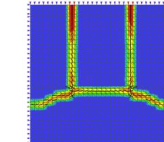
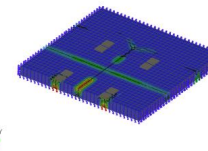
No.	Specimens Name	Finite Element Cracks Pattern	
27	R27-P250-0-45 $f_c$ : 45 MPa t: 250 mm $V_f$ : 0%		
28	R28-H150-0.68-45 $f_c$ : 45 MPa t: 150 mm $V_f$ : 0.68 + 0.2%		
29	R29-H200-0.68-45 $f_c$ : 45 MPa t: 200 mm $V_f$ : 0.68 + 0.2%		
30	R30-H250-0.68-45 $f_c$ : 45 MPa t: 250 mm $V_f$ : 0.68 + 0.2%		
31	R31-H150-0.8-45 $f_c$ : 45 MPa t: 150 mm $V_f$ : 0.8 + 0.2%		

Table A2. Cont.

No.	Specimens Name	Finite Element Cracks Pattern	
32	R32-H200-0.8-45 $f_c$ : 45 MPa t: 200 mm $V_f$ : 0.8 + 0.2%		
33	R33-H250-0.8-45 $f_c$ : 45 MPa t: 250 mm $V_f$ : 0.8 + 0.2%		
34	R34-H150-0.96-45 $f_c$ : 45 MPa t: 150 mm $V_f$ : 0.96 + 0.2%		
35	R35-H200-0.96-45 $f_c$ : 45 MPa t: 200 mm $V_f$ : 0.96 + 0.2%		
36	R36-H250-0.96-45 $f_c$ : 45 MPa t: 250 mm $V_f$ : 0.96 + 0.2%		

## References

1. Nie, Q.; Zhou, C.; Li, H.; Shu, X.; Gong, H.; Huang, B. Numerical simulation of fly ash concrete under sulfate attack. *Constr. Build. Mater.* **2015**, *84*, 261–268. [[CrossRef](#)]
2. Wang, H.; Ozer, H.; Al-Qadi, I.L.; Duarte, C.A. Analysis of near-surface cracking under critical loading conditions using uncracked and cracked pavement models. *J. Transp. Eng.* **2013**, *139*, 992–1000. [[CrossRef](#)]
3. Zhou, C.; Lan, G.; Cao, P.; Tang, C.; Cao, Q.; Xu, Y.; Feng, D. Impact of freeze-thaw environment on concrete materials in two-lift concrete pavement. *Constr. Build. Mater.* **2020**, *262*, 120070. [[CrossRef](#)]
4. Chaddha, S.; Chauhan, A.S.; Chawla, B. A study on the rigid pavement construction, joint and crack formation. *Int. J. Mod. Trends Eng. Res.* **2017**, *4*, 138–143.
5. Alkasah, İ. Hybrid Pavement: Assessment of Rigid and Flexible Pavements Together. Master's Thesis, Karabük University, Karabük, Turkey, 2020.
6. Bentur, A.; Mindess, S. *Fibre Reinforced Cementitious Composites*; CRC Press: Boca Raton, FL, USA, 2006.
7. Ghazy, A.; Bassuoni, M.T.; Maguire, E.; O'Loan, M. Properties of fiber-reinforced mortars incorporating nano-silica. *Fibers* **2016**, *4*, 6. [[CrossRef](#)]
8. Thirupathi, N.; Naresh, T.; Harish, B. The behaviour of rigid pavement by nonlinear finite element method. *J. Archit. Technol.* **2019**, *11*, 1–5.
9. Li, B.; Chi, Y.; Xu, L.; Shi, Y.; Li, C. Experimental investigation on the flexural behavior of steel-polypropylene hybrid fiber reinforced concrete. *Constr. Build. Mater.* **2018**, *191*, 80–94. [[CrossRef](#)]
10. Ibrahim, I.S.; Wan Jusoh, W.A.; Mohd Sam, A.R.; Mustapa, N.A.; Sk Abdul Razak, S.M. The mechanical properties of steel-polypropylene fibre composites concrete (HyFRCC). *Appl. Mech. Mater.* **2015**, *773–774*, 949–953. [[CrossRef](#)]
11. Liu, F.; Ding, W.; Qiao, Y. Experimental investigation on the flexural behavior of hybrid steel-PVA fiber reinforced concrete containing fly ash and slag powder. *Constr. Build. Mater.* **2019**, *228*, 116706. [[CrossRef](#)]
12. Shi, X.; Park, P.; Rew, Y.; Huang, K.; Sim, C. Constitutive behaviors of steel fiber reinforced concrete under uniaxial compression and tension. *Constr. Build. Mater.* **2020**, *233*, 117316.
13. Shan, L.; Zhang, L.; Xu, L.H. Experimental investigations on mechanical properties of hybrid steel-polypropylene fiber-reinforced concrete. *Appl. Mech. Mater.* **2014**, *638–640*, 1550–1555. [[CrossRef](#)]
14. Atiş, C.D.; Karahan, O. Properties of steel fiber reinforced fly ash concrete. *Constr. Build. Mater.* **2009**, *23*, 392–399. [[CrossRef](#)]
15. Karahan, O.; Atiş, C.D. The durability properties of polypropylene fiber reinforced fly ash concrete. *Mater. Des.* **2011**, *32*, 1044–1049. [[CrossRef](#)]
16. Zhang, P.; Li, Q.-f. Effect of polypropylene fiber on durability of concrete composite containing fly ash and silica fume. *Compos. Part B Eng.* **2013**, *45*, 1587–1594. [[CrossRef](#)]
17. Ali, B.; Qureshi, L.A.; Shah, S.H.A.; Rehman, S.U.; Hussain, I.; Iqbal, M. A step towards durable, ductile and sustainable concrete: Simultaneous incorporation of recycled aggregates, glass fiber and fly ash. *Constr. Build. Mater.* **2020**, *251*, 118980. [[CrossRef](#)]
18. Koushkbaghi, M.; Kazemi, M.J.; Mosavi, H.; Mohseni, E. Acid resistance and durability properties of steel fiber-reinforced concrete incorporating rice husk ash and recycled aggregate. *Constr. Build. Mater.* **2019**, *202*, 266–275. [[CrossRef](#)]
19. Ali, B.; Raza, S.S.; Hussain, I.; Iqbal, M. Influence of different fibers on mechanical and durability performance of concrete with silica fume. *Struct. Concr.* **2021**, *22*, 318–333. [[CrossRef](#)]
20. Wang, J.; Dai, Q.; Si, R.; Ma, Y.; Guo, S. Fresh and mechanical performance and freeze-thaw durability of steel fiber-reinforced rubber self-compacting concrete (SRSCC). *J. Clean. Prod.* **2020**, *277*, 123180. [[CrossRef](#)]
21. Shakir, H.M.; Al-Tameemi, A.F.; Al-Azzawi, A.A. A review on hybrid fiber reinforced concrete pavements technology. *J. Phys. Conf. Ser.* **2021**, *1895*, 012053. [[CrossRef](#)]
22. Pourreza, R. Investigating the Effects of Hybrid Fibres on the Structural Behaviour of Two-Way Slabs. Master's Thesis, Memorial University of Newfoundland, St. John's, NL, Canada, 2014.
23. Banthia, N.; Gupta, R. Hybrid fiber reinforced concrete (HyFRC): Fiber synergy in high strength matrices. *Mater. Struct.* **2004**, *37*, 707–716. [[CrossRef](#)]
24. Cominoli, L.; Failla, C.; Plizzari, G. Steel and synthetic fibres for enhancing concrete toughness and shrinkage behaviour. In Proceedings of the International Conference of Sustainable Construction Materials and Technologies, Coventry, UK, 11–13 June 2007; pp. 11–13.
25. Zongcai, D.; Jianhui, L. Mechanical behaviors of concrete combined with steel and synthetic macro-fibers. *Int. J. Phys. Sci.* **2006**, *1*, 57–66.
26. Khitab, A.; Arshad, M.T.; Hussain, N.; Tariq, K.; Ali, S.A.; Kazmi, S.; Munir, M. Concrete reinforced with 0.1 vol% of different synthetic fibers. *Life Sci. J.* **2013**, *10*, 934–939.
27. Hwang, J.-H.; Lee, D.H.; Ju, H.; Kim, K.S.; Seo, S.-Y.; Kang, J.-W. Shear behavior models of steel fiber reinforced concrete beams modifying softened truss model approaches. *Materials* **2013**, *6*, 4847–4867. [[CrossRef](#)] [[PubMed](#)]
28. Tabatabaei, Z.S.; Volz, J.S.; Keener, D.I.; Gliha, B.P. Comparative impact behavior of four long carbon fiber reinforced concretes. *Mater. Des.* **2014**, *55*, 212–223. [[CrossRef](#)]
29. Raza, S.S.; Qureshi, L.A.; Ali, B.; Raza, A.; Khan, M.M.; Salahuddin, H. Mechanical properties of hybrid steel-glass fiber-reinforced reactive powder concrete after exposure to elevated temperatures. *Arab. J. Sci. Eng.* **2020**, *45*, 4285–4300. [[CrossRef](#)]
30. Afroz, M.; Venkatesan, S.; Patnaikuni, I. Effects of hybrid fibers on the development of high volume fly ash cement composite. *Constr. Build. Mater.* **2019**, *215*, 984–997. [[CrossRef](#)]

31. Lau, C.K.; Chegenizadeh, A.; Htut, T.N.; Nikraz, H. Performance of the steel fibre reinforced rigid concrete pavement in fatigue. *Buildings* **2020**, *10*, 186. [[CrossRef](#)]
32. Hussain, I.; Ali, B.; Akhtar, T.; Jameel, M.S.; Raza, S.S. Comparison of mechanical properties of concrete and design thickness of pavement with different types of fiber-reinforcements (steel, glass, and polypropylene). *Case Stud. Constr. Mater.* **2020**, *13*, e00429. [[CrossRef](#)]
33. Abdulridha, M.A.; Salman, M.M.; Banyhussan, Q.S. Effect polypropylene of fiber on drying shrinkage cracking of concrete pavement using response surface methodology. *J. Eng. Sustain. Dev.* **2021**, *25*, 10–21. [[CrossRef](#)]
34. Zokaei, M.; Fakhri, M.; Rahiminezhad, S. A parametric study of jointed plain concrete pavement using finite element modeling. *Mod. Appl. Sci.* **2017**, *11*, 75–84. [[CrossRef](#)]
35. Tabatabaie, A.M.; Barenberg, E.J. Structural analysis of concrete pavement systems. *Transp. Eng. J. ASCE* **1980**, *106*, 493–506. [[CrossRef](#)]
36. Tayabji, S.D.; Colley, B.E. *Analysis of Jointed Concrete Pavements*; Tech. Rep. FHWS-RD-86-041; Federal Highway Administration: Washington, DC, USA, 1986.
37. Belletti, B.; Cerioni, R.; Meda, A.; Plizzari, G. Experimental and numerical analyses of FRC slabs on grade. In Proceedings of the FRAMCOS5 Conference, Vail, CO, USA, 12–16 April 2004; pp. 973–980.
38. Khan, M.I.; Khan, A.A.; Yadav, S. Mechanistic Analysis of Rigid Pavement for Wheel Load Stresses by Finite Element Method Considering Different Sub-Grade with Different Percentage of Metal Fibre. *Int. J. Eng. Trends Technol.* **2018**, *55*, 61–67. [[CrossRef](#)]
39. Zimmer, J.; Klein, D.; Stommel, M. Experimental and Numerical Analysis of Liquid-Forming. *Key Eng. Mater.* **2015**, 651–653, 842–847. [[CrossRef](#)]
40. Elnaga, I.M.A. Using of finite element in developing a new method for rigid pavement analysis. *Int. J. Civ. Eng. Technol.* **2014**, *5*, 69–75.
41. Trujillo, P.B.; Guerrero, M.A.S. Effect of temperature gradients on the behaviour of jointed plain concrete pavements. *Rev. IBRACON Estrut. E Mater.* **2019**, *12*, 398–407. [[CrossRef](#)]
42. Packard, R.G. *Thickness Design for Concrete Highway and Street Pavements*; Canadian Portland Cement Association: Ottawa, ON, Canada, 1984.
43. Huang, Y.H. *Pavement Analysis and Design*; Pearson: London, UK, 2004.
44. Garber, N.J.; Hoel, L.A. *Traffic and Highway Engineering*; Cengage Learning: Boston, MA, USA, 2019.
45. Sadeghi, V.; Hesami, S. Investigation of load transfer efficiency in jointed plain concrete pavements (JPCP) using FEM. *Int. J. Pavement Res. Technol.* **2018**, *11*, 245–252. [[CrossRef](#)]
46. Jafarifar, N. Shrinkage Behaviour of Steel-Fibre-Reinforced-Concrete Pavements. Ph.D. Thesis, University of Sheffield, Sheffield, UK, 2012.
47. Congress, I.R. *Guidelines for the Design of Plain Jointed Rigid Pavements for Highways*; IRC 58-2002; The Indian Roads Congress: New Delhi, India, 2002.
48. Shoukry, S.N.; Fahmy, M.; Prucz, J.; William, G. Validation of 3DFE analysis of rigid pavement dynamic response to moving traffic and nonlinear temperature gradient effects. *Int. J. Geomech.* **2007**, *7*, 16–24. [[CrossRef](#)]
49. Das, A. *Analysis of Pavement Structures*; CRC Press: Boca Raton, FL, USA, 2014.
50. Mahrenholtz, O.H. Beam on viscoelastic foundation: An extension of Winkler’s model. *Arch. Appl. Mech.* **2010**, *80*, 93–102. [[CrossRef](#)]
51. Kausel, E. Early history of soil–structure interaction. *Soil Dyn. Earthq. Eng.* **2010**, *30*, 822–832. [[CrossRef](#)]
52. Ioannides, A.M. Concrete pavement analysis: The first eighty years. *Int. J. Pavement Eng.* **2006**, *7*, 233–249. [[CrossRef](#)]
53. Westergaard, H.M. *Stresses in Concrete Pavements Computed by Theoretical Analysis*; Public Roads; Federal Highway Administration: Washington, DC, USA, 1926.
54. Cervenka, V.; Jendele, L.; Cervenka, J. *ATENA Program Documentation. Part 1. Theory*; Cervenka Consulting: Prague, Czech Republic, 2020; 344p.
55. Cervenka, V.; Cervenka, J.; Janda, Z.; Pryl, D. *ATENA Program Documentation, Part 8: User’s Manual for ATENA-GiD Interface*; Cervenka Consulting: Prague, Czech Republic, 2017.
56. Sorelli, L.G.; Meda, A.; Plizzari, G.A. Steel fiber concrete slabs on ground: A structural matter. *ACI Mater. J.* **2006**, *103*, 551–558.
57. Shakir, H.M.; Al-Azzawi, A.A.; Al-Tameemi, A.F. Nonlinear Finite Element Analysis of Fiber Reinforced Concrete Pavement under Dynamic Loading. *J. Eng.* **2022**, *28*, 81–98. [[CrossRef](#)]